Journal of Computational Physics 229 (2010) 2999–3018

Contents lists available at ScienceDirect

Journal of Computational Physics

journal homepage: www.elsevier.com/locate/jcp

A hybrid, center-difference, limiter method for simulations of compressible multicomponent flows with Mie-Grüneisen equation of state

G.M. Ward *, D.I. Pullin

Graduate Aeronautical Laboratories, California Institute of Technology, Mail Code 205-45, Caltech, Pasadena, CA 910.525/910.506, USA

ARTICLE INFO

Article history:
Received 29 July 2009
Received in revised form 9 November 2009
Accepted 21 December 2009
Available online 4 January 2010

Keywords:
Hybrid methods
Center difference
Limiter methods
Weighted essentially non-oscillatory methods
Mie-Grüneisen equation of state

ABSTRACT

We develop an efficient spatially high-order, Cartesian-mesh, hybrid, center-difference, limiter methodology for numerical simulations of compressible multicomponent flows with isotropic Mie-Grüneisen equation of state. Effective switching between center-difference and limiter schemes is achieved by a set of robust tolerance and Lax-entropy based criterion [18]. Oscillations that could result from a mixed stencil scheme are minimized by requiring that the limiter method approaches the center-difference method in smooth regions. To achieve this the limiter is based on a norm of the deviation of WENO reconstruction weights from ideal. Results from a spatially 4th order version of the methodology are presented in one and two dimensions utilizing the California Institute of Technology's VTF (Virtual Test Facility) AMROC [7] software.

1. Introduction

In the presence of shocks and interfaces, compressible flows involve both smooth and nearly discontinuous features. Adequate treatment of such features is best achieved by different schemes. In smooth regions a low-numerical dissipation skew-symmetric kinetic-energy preserving scheme is desirable and can be achieved by a low-cost center-difference method. Alternatively, though generally more numerically expensive, at shocks and sharp interfaces it is desirable to have a scheme with sufficient upwinding to prevent oscillations. Hybrid methodology therefore presents an effective approach to improving overall solver performance by selectively applying schemes to different regions. Furthermore, the ability to achieve low dissipation in smooth regions of flow is of primary interest when applying explicit turbulence models [2,10,24,19]. Proper creation of such a hybrid of scheme is not trivial and requires special attention to detail. In general no guarantee of stability can be made. Additionally, differences in dispersion relation can cause spurious oscillations and large errors in regions where schemes meet and switch.

Constructing a hybrid solver that combines center-difference and upwinding methods for multiphase flows with Mie-Grüneisen equations of state poses a special challenge in that the typically applied flux-splitting WENO reconstruction approach fails to prevent catastrophic oscillations at contacts. For perfect gases a substantial literature on hybrid solvers exists focusing on the use of such WENO solvers [2,10,24] while not addressing this problem. These reconstruct fluxes directly, employing a flux-splitting approach that maintains global conservation. These conservative WENO methods have great appeal for building hybrid solvers in that they allow for the choice of an ideal stencil in smooth regions of a solution, constructing the ideal stencil from a smoothness dependent weighting of sub stencils. This allows for the dispersion relationship of the two schemes used in a hybrid scheme to be matched for small wave numbers [10]. Although smooth transition between schemes is achieved, a significant short-coming of such conservative solvers is that catastrophic oscillations can develop

* Corresponding author.
E-mail address: geoff@caltech.edu (G.M. Ward).

0021-9991/$ - see front matter © 2010 Elsevier Inc. All rights reserved.
doi:10.1016/j.jcp.2009.12.027

in multicomponent mixtures [1]. A primitive WENO reconstruction based Roe Riemann solver [27] has been developed by Johnsen and Colonius [12] that prevents such oscillations in mixtures of perfect gases. However, the stencil associated with any such Riemann solver is dependent on the flow locally and therefore the dispersion relation is complex and does not lend itself to hybrid methodology. For multiphase flows with Mie-Grüneisen equations of state, Miller and Puckett [21] developed a volume of fluid approach that utilizes an approximate Riemann solver, again yielding no ideal stencil for smooth flows. Likewise, Shyue [31] has extended Roe's approximate Riemann solver for multiphase Mie-Grüneisen flows. Simplistic attempts to form hybrid solvers by low-order smoothness measure based blending of schemes have been made for conservative flux-splitting solvers [2,24].

Presently, in order to address the above issues, we construct a more rigorous blending methodology based on a norm of the deviation of local smoothness dependent WENO reconstruction weights. In devising our limiter we draw on similarities between WENO and classical flux and slope limiter type methods, providing practical insight. Doing so yields a generalized limiter useful for smoothly blending a lower order upwinding Riemann solver and high-order center-difference scheme while maintaining high-order convergence for smooth flows. We first apply the limiter methodology to the linear advection equation, building 4th- and 6th-order schemes and providing comparison to standard 3rd- and 5th-order WENO methods. We proceed to give a detailed description of a spatially 4th-order finite difference patch solver for the multiphase Euler equations with special consideration for the Mie-Grüneisen equation of state. The implementation combines spatially 4th-order, skew-symmetric, kinetic-energy preserving center-difference and a 2nd-order WENO-Roe Riemann approach. Hybridization is achieved for the solver through Lax-entropy conditions and gradient tolerances. We initially demonstrate the new scheme for solids modeled by isotropic Mie-Grüneisen equations of state in one dimension. We follow up by applying the methodology in two dimensions with adaptive mesh refinement capabilities utilizing the California Institute of Technology's VTF AMROC software [7].

2. Equation of state background

We begin by providing background on isotropic Mie-Grüneisen equations of state for solids. In a completely general manner, an isotropic equation of state can be rigorously constructed about a parametric reference state curve through an integral equation. Choosing to construct pressure as a function of internal energy and density leads to the very convenient Mie-Grüneisen formalism

$$p(\rho,e) = p_{ref}(\rho) + \rho \int_{e_{ref}(\rho)}^{e} \Gamma(\rho,e')de', \tag{1}$$

where $p_{ref}(\rho)$ and $e_{ref}(\rho)$ form a density parameterized reference state curve and $\Gamma(\rho,e)$ is the Grüneisen parameter defined by

$$\Gamma(\rho,e) = \frac{1}{\rho}\left.\frac{\partial p}{\partial e}\right|_{\rho}. \tag{2}$$

Any given material is then well defined thermodynamically by $p_{ref}(\rho), e_{ref}(\rho)$, and $\Gamma(\rho,e)$. In practice, whether analytic or tabulated, these three functions should, at a minimum, result in the thermodynamic stability of the material modeled in state regions of interest [21].

2.1. Hugoniots as reference state curves

For the simulation of compressible flows involving shocks it is convenient to use shock-Hugoniots for reference state curves. For many solids of interest, starting from state ρ_0, p_0, e_0, experimental data indicates that over a large range of shock strengths the relationship between shock and particle speed is adequately approximated by a simple linear fit

$$u_s = c_0 + \sigma u_p, \tag{3}$$

where u_s is the shock's speed, u_p is the post-shock-particle speed, c_0 is the unshocked medium's speed of sound, and σ is related to the unshocked medium's isentropic derivative of the bulk modulus K_s with respect to pressure

$$\begin{aligned} K_s &= \left.\frac{\partial Ln(p)}{\partial \rho}\right|_s, \\ \sigma &= \left(\left.\frac{\partial K_s}{\partial p}\right|_s + 1\right)\Big/ 4. \end{aligned} \tag{4}$$

Utilizing (3) and the three Rankine–Hugoniot jump conditions for conservation of mass, momentum, and energy,

$$\begin{aligned} \rho &= \rho_0 u_s/(u_s - u_p), \\ p &= p_0 + \rho_0 u_s u_p, \\ e &= e_0 + \frac{1}{2}(p + p_0)(1/\rho_0 - 1/\rho), \end{aligned} \tag{5}$$

results in the internal pressure and energy parametrized as functions of density along the shock-Hugoniot,

$$p_H(\rho) = p_0 + \frac{c_0^2(1/\rho_0 - 1/\rho)}{[1/\rho_0 - \sigma(1/\rho_0 - 1/\rho)]^2}, \tag{6}$$

$$e_H(\rho) = e_0 + \frac{1}{2}(p_H(\rho) + p_0)(1/\rho_0 - 1/\rho). \tag{7}$$

Additionally, for many solids it is found that the Grüneisen parameter is well approximated by

$$\Gamma(\rho, e) = \Gamma_0 \left(\frac{\rho_0}{\rho}\right)^q = \Gamma_H(\rho). \tag{8}$$

In terms of internal energy this is a 1st order approximation to $\Gamma(\rho, e)$ near the Hugoniot:

$$\Gamma(\rho, e) = \Gamma(\rho, e_H(\rho)) + \left.\frac{\partial \Gamma}{\partial e}\right|_{\rho, e_H(\rho)} (e - e_H(\rho)) + \cdots = \Gamma_H(\rho) + O(\Delta e). \tag{9}$$

Thus we have an equation of state that is guaranteed to be at least 1st order in internal energy near the central Hugoniot with

$$p(\rho, e) = p_H(\rho) + \rho \Gamma_H(\rho)(e - e_H(\rho)). \tag{10}$$

Generally, (6) and (7) are only valid for compressed states $\rho > \rho_0$. For expanded states a 2nd order isentropic continuation to the Hugoniot known as a Murnaghan isentrope is sometimes used [21]:

$$p_H(\rho) = \left(p_0 + \frac{\rho_0 c_0^2}{4\sigma - 1}\right)\left(\frac{\rho}{\rho_0}\right)^{4\sigma - 1} - \frac{\rho_0 c_0^2}{4\sigma - 1}, \tag{11}$$

$$e_H(\rho) = e_0 + \int_{\rho_0}^{\rho} \frac{p_H(\rho)}{\rho^2} d\rho. \tag{12}$$

2.2. Equation of state limitations

Construction of a central Hugoniot utilizing the assumption of a linear shock-particle speed relationship and Murnaghan isentrope extension for expanded states result in two notable limitations. First, using a simple linear fit to the relationship between shock and particle speed causes a singularity in the equation of state that results in a nonphysical maximum density

$$\rho_{max} = \frac{\rho_0}{1 - 1/\sigma}, \tag{13}$$

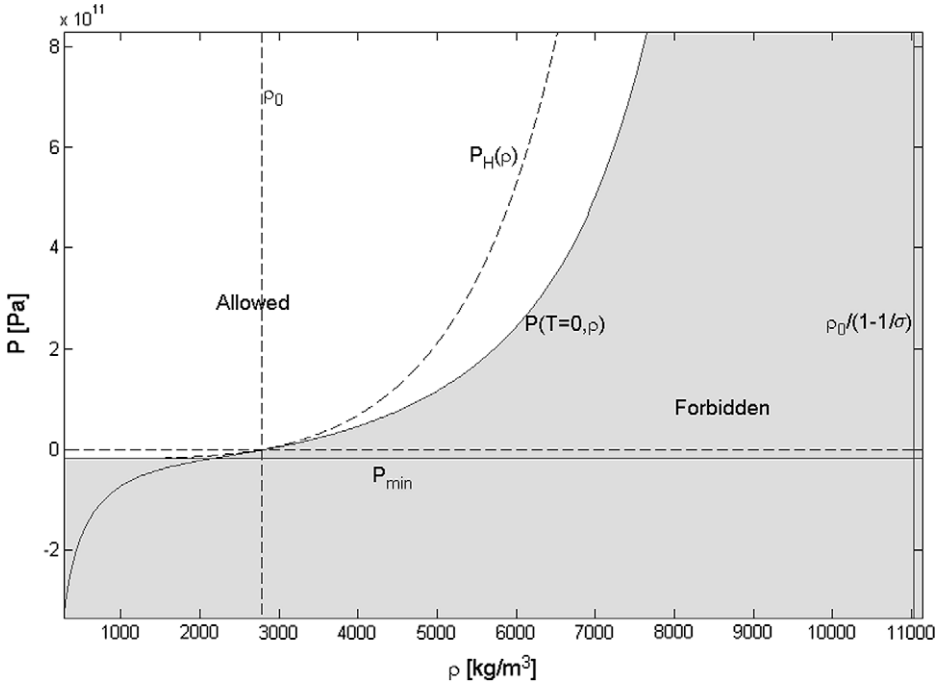

Fig. 1. Forbidden and allowed state regions for Aluminum modeled by a Mie-Grüneisen equation of state with a shock-Hugoniot reference state curve. The available states are bounded by negative temperature, a nonphysical minimum pressure $p_{min} = \frac{-\rho_0 c_0^2}{4\sigma - 1}$, and a nonphysical maximum density $\rho_{max} = \frac{\rho_0}{1 - 1/\sigma}$.

when $\sigma > 1$, as is typical for solids. Second, analysis of isentropes created by the extension of the Hugoniot for expanded states via the Murnaghan isentrope demonstrates a nonphysical minimum pressure:

$$\left.\frac{dp}{d\rho}\right|_s = c_1\frac{p}{\rho^2} + c_2\frac{1}{\rho^2} + c_3\rho^{4\sigma-3} + c_4\rho^{4\sigma-2} \tag{14}$$

along any isentrope when $\rho < \rho_0$ and $p < p_0$, where c_1, c_2, c_3, and c_4 depend on the central Hugoniot constants. Integrating (14) from initial conditions ρ_i, p_i, and s_i yields

$$p(\rho, s_i) = \left(p_i + \frac{c_2}{c_1}\right)e^{c_1(1/\rho_i - 1/\rho)} - \frac{c_2}{c_1} + e^{c_1/\rho}\int_{\rho_i}^{\rho}\left(c_3\rho'^{4\sigma-3} + c_4\rho'^{4\sigma-2}\right)e^{c_1/\rho'}\,d\rho'. \tag{15}$$

When approached from the part of the $p-\rho$ plane of physical interest, the limit

$$\lim_{\rho\to 0} p(\rho, s_i) \to -\frac{c_2}{c_1} = \frac{-\rho_0 c_0^2}{4\sigma - 1} \tag{16}$$

is obtained for all associated isentropes when $\sigma > 1/2$. Therefore no pressures lower than

$$p_{min} = \frac{-\rho_0 c_0^2}{4\sigma - 1} \tag{17}$$

are attainable. With $\rho_0 > 0, c_0 > 0$, and $\sigma > 0$ it is clear that $p_{min} < 0$ is typical and therefore negative pressure or tension is permissible. It is useful to place a tensile strength limitation when tension is expected in a simulation. Additionally, positivity of absolute temperature must not be violated. Taking constant specific heat for Aluminum yields Fig. 1, giving some face to the expected $p-\rho$ plane of validity.

2.3. Mixture rules

Kinetic theory for ideal gas mixtures predicts that total pressure is described by partial pressure summation. For mixtures of distinct ideal gases this law is easily applied to form an analytic equation of state. However, for most materials such a simple theory for molecular interactions in mixtures does not exist. Owing to the complexity inherent in providing a physical mixture model for real materials, previous works addressing the simulation of multiphase flows typically ignore the topic and assume discontinuous contact between materials, either tracking the contact [21] or smearing it with an ad hoc mixture rule [3,31] such as a level set, ψ, average of parameters

$$x_0^{mix} = \sum_{i=1}^{n}\psi_0^i x_0^i, \quad x \to \rho_0, p_0, e_0, \ldots \tag{18}$$

To do better would, at a minimum, require knowledge of $\rho_0, p_0, e_0, \ldots$ as a function of initial volume or mass fraction, data that is typically not available. In light of the complexity of the physics of mixtures, the ad hoc mixture rule (18) will be utilized presently because of its overall simplicity and robustness.

3. Hybrid limiter methodology

Hyperbolic conservation laws typically describe material behavior containing discontinuities and smooth regions, two features best addressed by different numerical schemes. At discontinuities a low-order upwinding scheme is ideal for preventing oscillations. Alternatively, in smooth regions of the solution a low dissipation method, often in the form of a centered difference scheme, is advantageous [2,10,24]. However, applying different schemes directly to different regions can lead to oscillations in regions where schemes meet if their dispersion relations are not suitably well matched [10]. To avoid this difficulty, it is important that the stencil associated with one of the schemes tends toward the others in regions where the schemes will meet. Additionally, flows with mixtures of real materials modeled by Mie-Grüneisen equations of state can develop disastrous oscillations when treated numerically by a conservative flux-splitting numerical scheme [1]. A generalized limiter approach presents a way to address the above issues simultaneously. In practice the success depends heavily on how the limiter is defined. Typically the limiter is based on a measure of smoothness locally. In reality it is difficult to achieve the desired result of the limiter method completely reducing to the desired stencil. For this reason a separate set of criterion resulting in a sharp cutoff filtering of the limiter is of practical use. In effect, all hybrid schemes may be formulated as limiter schemes with sharp cutoff filtering of the limiter.

3.1. Limiter methodology

The Lax-Wendroff theorem [15,16,32] indicates proper weak solution convergence for hyperbolic conservation laws can only be obtained by using a numerical scheme that maintains conservation of certain variables. A practical approach to creating such a conservative scheme is to define flux derivatives by a symmetric difference of midpoint reconstructions $\hat{f}_{j+\pm 1/2}$ of order at least $k-2$,

$$\frac{\partial f}{\partial x} = \frac{\hat{f}_{j+1/2} - \hat{f}_{j-1/2}}{\Delta x} + O(\Delta x^k). \tag{19}$$

Although primitive quantities are not conserved, the above methodology can be applied uniformly in approximating all derivatives. Practical application of (19) then only requires a midpoint reconstruction of quantities of interest, namely fluxes and primitives.

A blending of multiple reconstruction schemes is appealing for achieving different stencils for sharp and smooth features:

$$\hat{f}_{j+1/2} = \hat{f}^k_{j+1/2} + \Phi\left(\hat{f}^r_{j+1/2} - \hat{f}^k_{j+1/2}\right). \tag{20}$$

Here Φ is a limiter used to achieve the desired blend of $\hat{f}^r_{j+1/2}$ and $\hat{f}^k_{j+1/2}$, rth and kth order midpoint reconstructions, respectively. Typically $\hat{f}^r_{j+1/2}$ is a low-order upwinding scheme and $\hat{f}^k_{j+1/2}$ is a higher order method with less dissipation ($k > r$). It is therefore desirable that Φ approaches unity at discontinuities and tends toward zero in smooth regions. Additionally, in order to maintain kth order global convergence when a smooth solution is present, it is important to use a limiter with the property that

$$\Phi \propto \Delta x^\beta, \quad \beta \geqslant k - r. \tag{21}$$

Defining a good limiter of practical use is a complicated matter [15,16,32]. In the following section we present a structured way to define a practical limiter for a kth order scheme based on WENO weights.

3.2. WENO weight inspired limiters

Weighted essentially non-oscillatory (WENO) schemes represent a popular subcategory of solvers for hyperbolic partial differential equations [17,11,29]. At a basic level of interpretation WENO is merely polynomial interpolation by weighted hierarchy. For practical application to numerical methods on evenly spaced Cartesian grid points, WENO focuses on the reconstruction of midpoint values, forming a weighted combination of r 1st-order sub stencil interpolations q^r_k that tend toward an order $2r-1$ approximation q^{2r-1}_{r-1} of function f at $x = (j+1/2)\Delta x$ in smooth regions:

$$f_{j+1/2} = q^{2r-1}_{r-1}(f_{j-r+1}, \ldots, f_{j+r-1}) + \sum_{k=0}^{r-1} (w_k - C^r_k) q^r_k(f_{j+k-r+1}, \ldots, f_{j+k}) = \sum_{k=0}^{r-1} w_k q^r_k(f_{j+k-r+1}, \ldots, f_{j+k}). \tag{22}$$

Here C_k represent ideal sub stencil weighting and w_k are variable weights dependent on local solution character. The above reflects a slope limiter-like approach to the reconstruction of midpoint values. Although not directly in slope limiter form, it is not to difficult to design weights that yield classic slope limiter or even ENO methods. More commonly weights are defined systematically by

$$w_k = \frac{\alpha_k}{\sum_{j=0}^{r-1} \alpha_j}, \tag{23}$$

$$\alpha_k = \frac{C^r_k}{(\epsilon + IS_k)^p}, \quad k = 0, 1, \ldots, r-1, \tag{24}$$

where IS_k is a sub stencil smoothness measure, p and ϵ are chosen constants, and C^r_k is the desired sub stencil weight in smooth solution regions [11].

Noting that slope and flux-limiter approaches are equivalent, it is instructive to re-arrange (22) in a flux-limiter-like form

$$f_{j+1/2} = q^{2r-1}_{r-1}(f_{j-r+1}, \ldots, f_{j+r-1}) + \sum_{k=0}^{r-2} \phi_k q^r_k(f_{j+k-r+1}, \ldots, f_{j+k}) - \sum_{k=0}^{r-2} \phi_k q^{2r-1}_{r-1}(f_{j-r+1}, \ldots, f_{j+r-1}). \tag{25}$$

A matrix relationship exists relating the flux-limiters ϕ_k and classic WENO weights w_k,

$$\underline{\underline{A}}(\underline{C}^r) \cdot \underline{\phi} = \underline{w} - \underline{C}^r. \tag{26}$$

Taking a norm of the above yields a single generalized limiter,

$$\Phi = \|A\|_p \| \|\underline{w} - \underline{C}^r\|_p. \tag{27}$$

It is not surprising that the limiter norm is directly proportional to a norm of the deviation of weights from ideal. Eq. (27) provides a generalized robust way for defining a limiter for high-order schemes.

4. High-order implementation

4.1. Linear advection equation solver

To demonstrate application of Eq. (27) we first apply the methodology to the linear advection equation,

$$\frac{\partial u}{\partial t}+\frac{\partial u}{\partial x}=0, \tag{28}$$

creating spatially 4th and 6th order schemes based on high-order center-differences and WENO reconstruction Riemann solvers.

In constructing a 4th-order method we utilize a standard 4th-order center-difference,

$$\hat{u}^{CD4}_{j+1/2}=-\frac{1}{12}(u_{j+2}+u_{j-1})+\frac{5}{12}(u_j+u_{j+1}), \tag{29}$$

combined by limiter with a 3rd-order WENO scheme $\hat{u}^{WENO3}_{j+1/2}$ [17],

$$\hat{u}_{j+1/2}=\hat{u}^{CD4}_{j+1/2}+\Phi\left(\hat{u}^{WENO3}_{j+1/2}-\hat{u}^{CD4}_{j+1/2}\right). \tag{30}$$

Where the limiter is defined by,

$$\Phi=\|\underline{w}-\underline{C}^r\|_2. \tag{31}$$

In evaluating the deviation norm of Eq. (31) we follow the approach of standard 5th order WENO with $r=3$ and the preferred stencil coefficients $C^3_0=1/10,\ C^3_1=6/10,\ C^3_2=3/10$. In determining the weights we follow [11], setting $\epsilon=10^{-6}, p=2$, and using the smoothness measures

$$\begin{aligned}
IS_0&=\frac{13}{12}(u_{j-2}-2u_{j-1}+u_j)^2+\frac{1}{4}(u_{j-2}-4u_{j-1}+3u_j)^2,\\
IS_1&=\frac{13}{12}(u_{j-1}-2u_j+u_{j+1})^2+\frac{1}{4}(u_{j-1}-u_{j+1})^2,\\
IS_2&=\frac{13}{12}(u_j-2u_{j+1}+u_{j+2})^2+\frac{1}{4}(3u_j-4u_{j+1}+3u_{j+2})^2.
\end{aligned} \tag{32}$$

Likewise, in constructing a 6th-order scheme we utilize the 6th-order center-difference,

$$\hat{u}^{CD6}_{j+1/2}=\frac{1}{60}(u_{j+3}+u_{j-2})-\frac{2}{15}(u_{j+2}+u_{j-1})+\frac{37}{60}(u_{j+1}+u_j), \tag{33}$$

and combine it by limiter with a 5th-order WENO method $\hat{u}^{WENO5}_{j+1/2}$ [11],

$$\hat{u}_{j+1/2}=\hat{u}^{CD6}_{j+1/2}+\Phi\left(\hat{u}^{WENO5}_{j+1/2}-\hat{u}^{CD6}_{j+1/2}\right). \tag{34}$$

It is possible to combine 6th-order center-difference with 3rd-order WENO scheme and still achieve 6th order convergence for smooth solutions. However, doing so results in higher dissipation at discontinuities. To construct Φ for the present 6th-order method from Eq. (27) we utilize 7th order WENO preferred stencil coefficients and smoothness indicators with $p=5$, for which the equations are omitted and can be found in their original source [4].

To form a complete numerical scheme from the above spatial discretization a temporal discretization is then required. For testing purposes, we apply 4th-order strong-stability preserving Runge–Kutta (SSP RK-4) temporal discretization [9],

$$\begin{aligned}
q^{(1)}&=q^n+\frac{1}{2}\Delta tL(q^n),\\
q^{(2)}&=q^n+\frac{1}{2}\Delta tL(q^{(1)}),\\
q^{(3)}&=q^n+\Delta tL(q^{(2)}),\\
q^{n+1}&=\frac{1}{3}(-q^n+q^{(1)}+2q^{(2)}+q^{(3)})+\frac{1}{6}\Delta tL(q^{(3)}),
\end{aligned} \tag{35}$$

4.2. Test problems

For the purposes of comparison we now apply the previously described 4th and 6th order methods, as well as 3rd and 5th order WENO methods, to the linear advection equation in a periodic domain $-1\leqslant x\leqslant 1$ with initial conditions

$$u(x,t=0)=\begin{cases}1, & -3/4<x<-1/4\\ e^{-300(x-0.5)^2}, & \text{otherwise.}\end{cases} \tag{36}$$

Numerical solutions are shown at the 2000th time step in Fig. 2 for simulation with $n=100$ points and $CFL=0.5$. The present 6th order scheme best captures the solution, retaining the Gaussian's peak with greater fidelity and having a slightly sharper approximation to the square wave. Third-order WENO displays a heavily diffuse approximation to the solution, yielding an approximation with the greatest L_2 norm error out of all methods presently examined.

For smooth solutions the convergence rate is simply the order of the method. For hyperbolic partial differential equations, convergence to weak solutions is of primary interest. To better compare the schemes we next performed a convergence

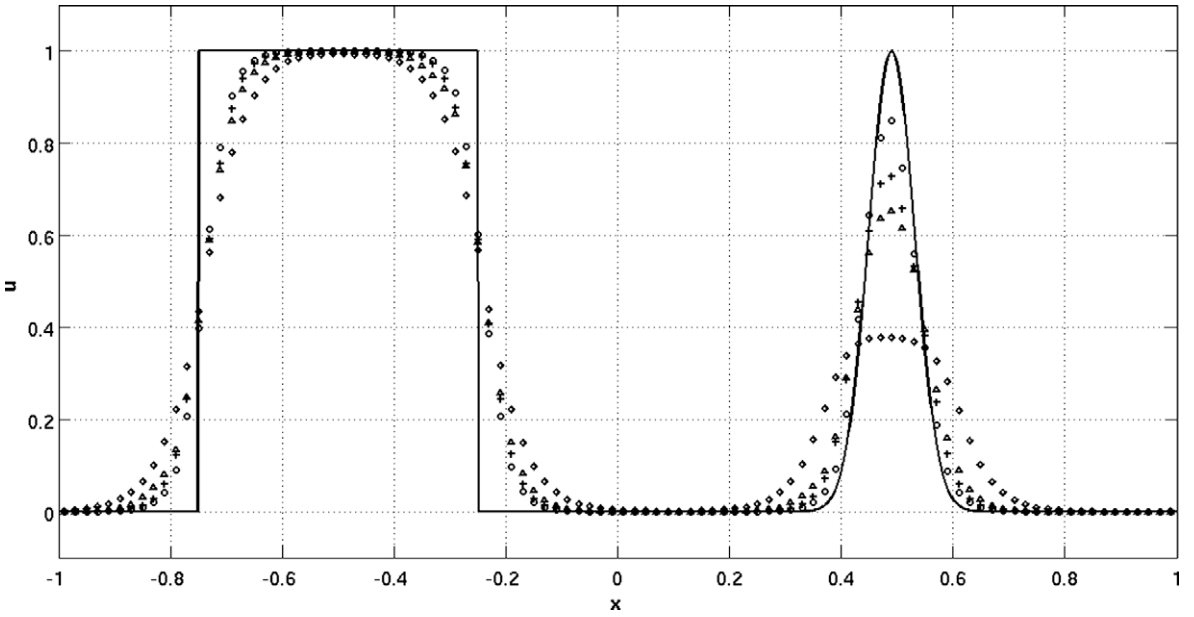

Fig. 2. Numerical solutions to the linear advection equation in a periodic domain achieved with spatially 3rd and 5th order WENO, present 4th and 6th order WENO inspired limiter methods, denoted by diamonds and crosses, triangles and circles, respectively. Solution depicted at 2000th time step, $CFL = 0.5$ and $n = 100$.

study for a square wave in a periodic domain. L_2 error norm and convergence rate results from the study are given in Table 1. To be consistent, for 5th-order WENO we take $\Delta t = (CFL \times \Delta x)^{5/4}$ and for our 6th-order method $\Delta t = (CFL \times \Delta x)^{3/2}$. The present 6th-order method demonstrates a slightly higher convergence rate to the weak solution then the others. The currently proposed 4th-order method demonstrates roughly the same convergence rate as that of 5th-order WENO, likely due to the limiter being based on 5th-order WENO weights.

4.3. Hybrid multiphase Euler solver for Mie-Grüneisen fluids

In the following sections we present a 4th-order spatial patch solver implementation of a WENO weight limiter based hybrid scheme applicable in up to three dimensions for multiphase flows with Mie-Grüneisen equations of state. Classic 4th-order, center-difference in a skew-symmetric formulation of the energy and momentum equations is used for the ideal stencil [23]. For the low-order upwinding solver a 3rd-order WENO reconstruction of primitives coupled with a Roe approximate Riemann solver is applied [31]. The limiter used is calculated from WENO weights associated with a 5th-order flux splitting approach [11]. Temporal discretization is performed by total variation diminishing third-order Runge–Kutta (TVD-RK3). Hybridization is achieved through a Lax-entropy and gradient tolerance based switching criterion [18,23]. The California Institute of Technology's VTF AMROC [7] software is used to apply this patch solver in up to two dimensions with AMR capability.

4.3.1. Euler compressible flow equations

The Euler equations of multicomponent compressible fluid mechanics model a very specific subgroup of flows of interest. Under the assumptions made, fluid motion is described by a set of coupled conservative hyperbolic partial differential equations

Table 1
Square wave L_2 error norm and convergence order for $t = 2$ and $CFL = 0.9$.

N	3rd order L_2 error	WENO L_2 order	5th order L_2 error	WENO L_2 order	4th order L_2 error	Limiter L_2 order	6th order L_2 error	Limiter L_2 order
40	0.218306	–	0.189875	–	0.195927	–	0.180998	–
80	0.171496	0.348180	0.143627	0.402720	0.149808	0.387200	0.134949	0.423568
120	0.148070	0.362235	0.122103	0.400422	0.127423	0.399164	0.113716	0.422196
160	0.133336	0.364332	0.108706	0.403973	0.113588	0.399497	0.100573	0.426928
200	0.122895	0.365437	0.099287	0.406142	0.103838	0.402224	0.091383	0.429473

$$\frac{\partial \mathbf{q}}{\partial t}+\frac{\partial \mathbf{F}(\mathbf{q})}{\partial x}+\frac{\partial \mathbf{G}(\mathbf{q})}{\partial y}+\frac{\partial \mathbf{H}(\mathbf{q})}{\partial z}=0, \tag{37}$$

where the directional fluxes F, G, and H are given by

$$\mathbf{F}(\mathbf{q})=\begin{pmatrix}\rho u\\ \rho u^2+p\\ \rho uv\\ \rho uw\\ u(\rho E+p)\\ \rho u\psi_1\\ \vdots\\ \rho u\psi_{n-1}\end{pmatrix},\quad \mathbf{G}(\mathbf{q})=\begin{pmatrix}\rho v\\ \rho vu\\ \rho v^2+p\\ \rho vw\\ v(\rho E+p)\\ \rho v\psi_1\\ \vdots\\ \rho v\psi_{n-1}\end{pmatrix},\quad \mathbf{H}(\mathbf{q})=\begin{pmatrix}\rho w\\ \rho wu\\ \rho wv\\ \rho w^2+p\\ w(\rho E+p)\\ \rho w\psi_1\\ \vdots\\ \rho w\psi_{n-1}\end{pmatrix}, \tag{38}$$

with conserved vector of state $\mathbf{q}$ defined by

$$\mathbf{q}=(\rho,\rho u,\rho v,\rho w,\rho E,\rho\psi_1,\ldots,\rho\psi_{n-1}). \tag{39}$$

Here $E=e+\frac{1}{2}(u^2+v^2+w^2)$ is the energy per unit mass and ψ_j represents a scalar quantity of interest associated with the flows jth component. In practice it is useful to track either the scalar mass fraction or a level set associated with each component.

4.3.2. Preventing pressure oscillations in mixtures

An important fundamental subset of solutions to the Euler equations are those for which pressure and velocity are constant for all time, such as the translation of a pressure matched material interface. Any solver of practical use should be able to maintain such conditions after each temporal advance of the solution. Designing a scheme that does so for multicomponent flows is not entirely trivial [1]. In practice the degree to which the integrity of such solutions is compromised varies with the material models. For perfect gases with similar specific heat ratios the degradation may be slow enough to neglect for some flows of interest. However, this is not the case in general, particularly for flows involving multiple solids modeled by Mie-Grüneisen equations of state. In addressing the issue here we follow the approach of Shyue [31], tracking three additional functions of density related to the Mie-Grüneisen equation of state for the mixture and re-writing the conserved scalar equation in primitive form

$$\begin{aligned}
&\frac{\partial}{\partial t}\left(\frac{1}{\Gamma_H}\right)+\mathbf{u}\cdot\nabla\left(\frac{1}{\Gamma_H}\right)=-\rho\chi_{\Gamma_H}\nabla\cdot\mathbf{u},\\
&\frac{\partial}{\partial t}\left(\frac{p_H}{\Gamma_H}\right)+\mathbf{u},\cdot\nabla\left(\frac{p_H}{\Gamma_H}\right)=-\rho\chi_{p_H}\nabla\cdot\mathbf{u},\\
&\frac{\partial}{\partial t}(\rho e_H)+\mathbf{u}\cdot\nabla(\rho e_H)=-\rho\chi_{e_H}\nabla\cdot\mathbf{u},\\
&\frac{\partial\psi_j}{\partial t}+\mathbf{u}\cdot\nabla(\psi_j)=0,\quad (j=1,2,\ldots,n-1),
\end{aligned} \tag{40}$$

where

$$\chi_{\Gamma_H}=-\Gamma'_H/\Gamma_H^2, \tag{41}$$

$$\chi_{p_H}=(\Gamma_H p'_H-\Gamma'_H p_H)/\Gamma_H^2, \tag{42}$$

$$\chi_{e_H}=e_H+\rho e'_H, \tag{43}$$

and prime quantities indicate derivative with respect to density. For example,

$$\Gamma'_H=\frac{d\Gamma_H}{d\rho}. \tag{44}$$

The new vector of state of interest is then

$$\mathbf{q}=(\rho,\rho u,\rho v,\rho w,\rho E,1/\Gamma_H,p_H/\Gamma_H,\rho e_H,\psi_1,\ldots,\psi_{n-1}). \tag{45}$$

Pressure can be obtained directly from the vector of state by the relationship

$$p=\left(\rho E-\frac{(\rho u)^2+(\rho v)^2+(\rho w)^2}{2\rho}+\frac{p_H}{\Gamma_H}-\rho e_H\right)\Big/\left(\frac{1}{\Gamma_H}\right) \tag{46}$$

and likewise the speed of sound is defined by

$$c^2 = \left.\frac{\partial p}{\partial \rho}\right|_s = \left.\frac{\partial p}{\partial \rho}\right|_e + \frac{p}{\rho^2}\left.\frac{\partial p}{\partial e}\right|_\rho = \Gamma_H(e + p/\rho + \chi_{p_H} - \chi_{e_H} - p\chi_{\Gamma_H}). \tag{47}$$

It is important to note that simply adding three redundant equations alone is not sufficient to guarantee the prevention of oscillations. Careful consideration of how rounding error is propagated for constant pressure-velocity solutions must be taken. In this case, a locally uniform numerical discretization of derivatives in (40) and the rest of the Euler equations yields ratios in (46) that maintain constant pressure [31].

4.3.3. Center difference

For our 4th-order, center-difference scheme, we use a kinetic-energy preserving skew-symmetric reconstruction of quantities [22,23]. To achieve this the end product of the difference of midpoint reconstructions must be consistent with skew-symmetric form of the momentum and energy equations,

$$\frac{\partial(\rho u v)}{\partial x} = \frac{1}{2}\frac{\partial(\rho u v)}{\partial x} + \frac{1}{2}\rho u\frac{\partial v}{\partial x} + \frac{1}{2}v\frac{\partial(\rho u)}{\partial x}, \tag{48}$$

$$\frac{\partial(\rho E + p)u}{\partial x} = \frac{1}{2}\frac{\partial(\rho e u)}{\partial x} + \frac{1}{2}\rho u\frac{\partial e}{\partial x} + \frac{1}{2}e\frac{\partial(\rho u)}{\partial x} + \frac{1}{2}u\frac{\partial(\rho u v)}{\partial x} + \frac{1}{2}\rho u v\frac{\partial u}{\partial x} + u\frac{\partial p}{\partial x} + p\frac{\partial u}{\partial x}. \tag{49}$$

Therefore, for product quantities in the above skew-symmetric equations, define their midpoint reconstruction by

$$\hat{fg}^{skew}_{j+1/2} = \frac{1}{2}\left(\hat{fg}^{div}_{j+1/2} + \hat{fg}^{prod}_{j+1/2}\right) \tag{50}$$

where

$$\hat{f}^{div}_{j+1/2} = \alpha(f_{j+2} + f_{j-1}) + (\alpha + \beta)(f_j + f_{j+1}) \tag{51}$$

and

$$\hat{fg}^{prod}_{j+1/2} = \beta(f_j g_{j+1} + f_{j+1} g_j) + \alpha(f_{j+2} g_j + f_{j-1} g_{j+1} + f_j g_{j+2} + f_{j+1} b_{j-1}). \tag{52}$$

All other quantities are reconstructed by the simple divergence formulation of (51). The choice of $\beta = 1/2 - 2\alpha$ and $\alpha = -1/12$ leads to 4th order finite differences. Alternatively, Hill and Pullin [10] have optimized β and α for the purpose of minimizing dissipation of turbulent kinetic-energy over a spectrum of scales for application with an explicit turbulence model.

4.3.4. WENO-Roe solver

Riemann solvers represent a popular subset of upwinding numerical methods for hyperbolic partial differential equations. The basic idea behind such solvers is to reconstruct midpoint fluxes through solution to a Riemann problem between biased interpolations of left and right states. In general, for nonlinear equations such as the Euler equations, solution to Riemann problems are complex and can only be solved numerically at great expense. Linearization of the Riemann problem therefore presents an attractive alternative for providing quick approximate solutions. However, producing a robust and meaningful linearization is not a straight forward task. For perfect gases Roe's approximate Riemann solver [27] provides a meaningful way to linearize the Riemann problem. Extension of the methodology for more general materials, such as metals described by Mie-Grüneisen equations of state, is not necessarily achievable analytically. Despite this drawback, a Roe like linearization remains useful, retaining a moderate level of robustness while reducing the overall cost associated with solving the Riemann problem [30,31]. In light of this, our approach to reconstructing midpoint quantities is as follows: First, apply a 3rd order single dimension WENO interpolation of primitives,

$$\mathbf{u} = (\rho, u, v, w, p, \Gamma_H, p_H, e_H, \psi_1, \ldots, \psi_{n-1}), \tag{53}$$

to form left and right states $\mathbf{q_L}$ and $\mathbf{q_R}$. Then, following the approach of Shyue [31] we approximate the zero-characteristic quantities associated with the Riemann problem between these states by Roe linearization, a process described in the remainder of this section in detail.

Linearization of the Riemann problem associated with a conservative hyperbolic partial differential equation is most easily achieved by considering the nonconservative form. For the multicomponent Euler equations,

$$\frac{\partial \mathbf{q}}{\partial t} + \mathbf{A}_F(\mathbf{q})\frac{\partial \mathbf{q}}{\partial x} + \mathbf{A}_G(\mathbf{q})\frac{\partial \mathbf{q}}{\partial y} + \mathbf{A}_H(\mathbf{q})\frac{\partial \mathbf{q}}{\partial z} = 0, \tag{54}$$

where $\mathbf{A}_F(\mathbf{q}), \mathbf{A}_G(\mathbf{q}), \mathbf{A}_H(\mathbf{q})$ are the Jacobian matrices defined by

$$\mathbf{A}_F(\mathbf{q}) = \frac{\partial \mathbf{F}(\mathbf{q})}{\partial \mathbf{q}}, \quad \mathbf{A}_G(\mathbf{q}) = \frac{\partial \mathbf{G}(\mathbf{q})}{\partial \mathbf{q}}, \quad \mathbf{A}_H(\mathbf{q}) = \frac{\partial \mathbf{H}(\mathbf{q})}{\partial \mathbf{q}}. \tag{55}$$

In approximating the solution to the Riemann problem between states $\mathbf{q_L}$ and $\mathbf{q_R}$ Roe [27] linearized the Jacobian, eigenvectors, and eigenvalues by a weighted average of fundamental quantities:

$$\hat{x} = \frac{\sqrt{\rho_L}x_L + \sqrt{\rho_R}x_R}{\sqrt{\rho_L} + \sqrt{\rho_R}}. \tag{56}$$

Shyue [31] has adapted Roe's linearization for application to multiphase flows with Mie-Grüneisen equations of state. We presently use his adaption of Roe's solver and proceed to describe the minimal necessary detail for understanding the solution of linear Riemann problems leading to midpoint value reconstruction.

For linear equations the solution of a Riemann problem consists of a series of discontinuous jumps across characteristic waves propagating at the rate of their eigenvalues λ. In practice the magnitude of the jumps can be determined by requiring conservation across all characteristic waves,

$$\mathbf{R}\alpha = q_R - q_L = \Delta q. \tag{57}$$

The approximate zero-characteristic state needed for obtaining midpoint quantities of interest is then

$$q^* = q_R - \mathbf{R}^{-1}\alpha^+ \tag{58}$$

$$= q_L + \mathbf{R}^{-1}\alpha^-, \tag{59}$$

where

$$\alpha_j^+ = \begin{cases} \alpha_j & \text{if } \lambda_j > 0 \\ 0 & \text{otherwise} \end{cases} \tag{60}$$

and

$$\alpha^- = \alpha - \alpha^+. \tag{61}$$

4.3.5. Limiter

It is not necessary to use the matrix norm $\|A\|_p$ in (27) explicitly. A constant of proportionality is acceptable,

$$\Phi_j = B\|\underline{w}_j - \underline{C}^r\|_p. \tag{62}$$

Here we take the $p = 2$, corresponding to the L_2 norm. It is of practical interest to limit the range of possible values of Φ,

$$\Phi_{min} \leqslant \Phi_j \leqslant \Phi_{max}. \tag{63}$$

The values of Φ_{min} and Φ_{max} should be chosen congruently with the constant of proportionality B in order to give the desired amount of dissipation. Too large a value of B will push the limiter beyond Φ_{max}, voiding any possibility of retaining the desired convergence rate in smooth flows. We find that $B \sim 1$ is typically adequate for maintaining $0 \leqslant \Phi_j \leqslant 1$. The upwinding scheme used along with shock strength and the equation of state are all contributing factors to the appropriate determination of a practical Φ_{max}.

In evaluating the deviation norm of Eq. (62) we again use the 5th order WENO approach in Eq. (32). We use density as the single variable by which to measure smoothness, which is generally robust, except in the rare case of a constant density discontinuity. It is important to note that (32) contain an asymmetric odd number of points about the midpoint $j + 1/2$. Therefore, if applied directly, solutions that should be symmetric under coordinate inversion would not sustain symmetry numerically. Limiter symmetry can be restored by noting that the above is actually Φ_j^+ and that a Φ_j^- also exist from a WENO reconstruction for the same midpoint based on $(j+1) - 1/2$. Taking the mean $\Phi_j = \frac{1}{2}\left(\Phi_j^- + \Phi_j^+\right)$ then eliminates limiter asymmetry.

4.3.6. Temporal discretization

In terms of simplicity and cost effectiveness, explicit Runge–Kutta temporal discretization present an ideal approach. Whereas upwinding methods generally remain stable with simple 1st order explicit time stepping when applied to hyperbolic partial differential equations, center-difference schemes require additional consideration for stability. Third-order or higher temporal discretization is in fact necessary [23]. Following Pantano et al. [23], we primarily utilize the storage efficient third order total variation diminishing (TVD) Runge–Kutta [9],

$$q^{(1)} = q^n + \frac{1}{2}\Delta t L(q^n), \quad q^{(2)} = \frac{3}{4}q^n + \frac{1}{4}q^{(1)} + \frac{1}{4}\Delta t L(q^{(1)}), \quad q^{n+1} = \frac{1}{3}q^n + \frac{2}{3}q^{(2)} + \frac{1}{6}\Delta t L(q^{(3)}). \tag{64}$$

4.3.7. Adaptive mesh refinement

We presently utilize the California Institute of Technology's VTF AMROC [7] software to extend our methodology for parallel AMR application. AMROC is based on the parallel block structured AMR algorithm of Berger and Oliger [6,5]. The approach divides the domain into patches of various spatial resolutions, interpolating boundary conditions between levels. The same solver is applied to each patch while maintaining a constant spatial to temporal refinement ratio. We find that extension of our method within this framework achieves a reasonable level of success. We note, however, that significant variation in numerical method cost can lead to severe loss in parallel performance efficiency for certain problems. Optimi-

zation of hybrid methods in an adaptive mesh refinement context presents an additional level of complexity for load balancing that is not addressed presently.

4.3.8. Hybrid switching criterion

In practice the limiter method described in previous sections will never result in the center-difference scheme. Furthermore, if applied uniformly in the domain the computational cost would remain the same at each point even if the lower order upwinding scheme is barely used and not truly necessary. Since the center-difference scheme is cheap computationally relative to the upwinding Roe Riemann solver, overall code efficiency can be improved by only applying the limiter method to regions identified to contain discontinuities. A variety of approaches for flagging regions with discontinuities have been developed in the hybrid literature [10,23]. Here we follow a Lax-entropy-based approach for detecting shocks [18], identifying regions of interest by checking for alignment of pressure and entropy gradients,

$$\left(\frac{(\rho u)_{j+1}-(\rho u)_j}{\rho_{j+1}-\rho_j}\right) \quad (p_{j+1}-p_j)<0, \tag{65}$$

and using a Mach-divergence tolerance criterion,

$$\left|\frac{u_{j+1}-u_j}{c_0}\right| > tol. \tag{66}$$

Regions with sharp scalar gradients are flagged by a simple gradient tolerance,

$$|\psi_{j+1}-\psi_j| > tol. \tag{67}$$

Typically tolerance values are on the order of a percent, corresponding to waves slightly stronger than weak shocks and scalar variations larger than those treatable by a center-difference. The above provides a fairly robust set of criterion for flagging regions in need of upwinding. Occasionally a sharp gradient not associated with a shock or scalar quantity may be present. In such cases curvature based detection may be used [10,23],

$$\frac{|q_{j+1}+q_{j-1}-2q_j|}{|q_{j+1}+q_{j-1}+2q_j|} > tol. \tag{68}$$

In general, determination of the best flagging criterion and associated tolerance value is solution and scheme dependent. To protect further against oscillations it is useful to flag several closest neighboring points. Additionally, when applied in an adaptive mesh context, oscillations can occur at coarse-fine boundaries, making it desirable to add dissipation locally by use of an upwinding method [23].

4.3.9. Carbuncle phenomenon

Structured grids can lead to carbuncle phenomenon when strong, slow moving discontinuities aligned with a structured grid are present [8,25,28]. The classic case of carbuncle phenomenon is observed for inviscid Mach 15.3 perfect gas flow around a cylinder. The source of the name carbuncle was taken from the nonphysical carbuncle shaped bow shock achieved. Directional dissipation variation leading to grid induced instability is widely accepted as the source [28]. In perfect gases the phenomenon is associated with strong shocks. More generally, the problem is a result of strong grid aligned gradients in wave speeds. In multicomponent flows with exotic equations of state it might be expected that carbuncle phenomenon occur more readily.

We have found that for single mode Mach 1.5 Richtmyer–Meshkov instability between mid-ocean ridge basalt (MORB) and Molybdenum modeled by a shock-Hugoniot Mie-Grüneisen equations of state, features indicative of a carbuncle phenomenon are present in the form of a notch at the spike tip (Fig. 3(a)). The simulation corresponds to a centerline single mode cosine perturbation of a MORB-Molybdenum contact with wavelength $\lambda = 0.5$ m and amplitude $h_0 = 0.05$ m. Initially the states on either side of the contact are in mechanical equilibrium, corresponding to ρ_0, p_0, and e_0 given in Table 2. A Mach 1.5 shockwave travels downward through the MORB, eventually reaching the diffuse zone where it deposit vorticity and yields transmitted and reflected shocks. The simulation is performed in a frame of reference corresponding to zero velocity after post shock-interface interaction when no interface perturbation is present.

A key characteristic of carbuncle phenomenon is sensitivity to grid-flow alignment. To demonstrate that the feature observed in Fig. 3(a) is nonphysical, we performed a simulation with a 45° rotation of the flow with respect to the grid. The results, seen in Fig. 3(b), show an alleviation of the notch as well as a considerable change in the general shape of contours, indicating significant dependence of dissipation on grid orientation.

Presently, to produce a fix for the carbuncle phenomenon we follow the approach of Sanders [28]. For approximate linearized Riemann solvers the local directional dissipation matrix is given by

$$M = R|\Lambda|R^{-1}. \tag{69}$$

To correct the problem, Sanders [28] adjusts the eigenvalues Λ in (69) by an amount equal to the maximum local grid variation in wave speed

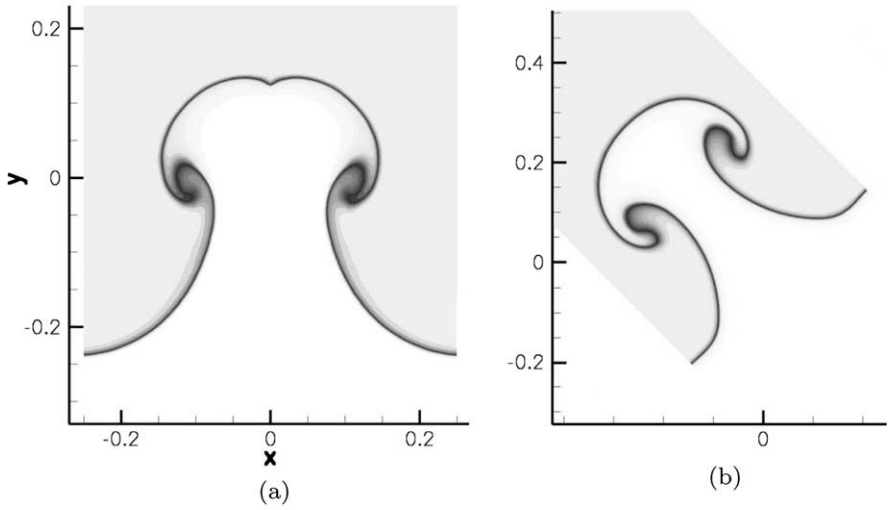

Fig. 3. MORB-Molybdenum Mach 1.5 single cosine mode perturbation Richtmyer–Meshkov instability simulation results exhibiting carbuncle like features ($t = 37$ ms). (a) A nonphysical notch at the spike tip is visible. (b) Rotating the flow by 45 degrees with respect to the grid removes the notch.

Table 2
Hugoniot constants for various materials.

	ρ_0	p_0	Γ_0	c_0	σ	q	T_0
Aluminum	2785 kg/m^3	0.0	2.0	5328 m/s	1.338	1.0	298 K
MORB	2660 kg/m^3	0.0	0.18	2100 m/s	1.68	1.0	1673 K
Molybdenum	9961 kg/m^3	0.0	1.56	4700 m/s	1.43	1.0	1673 K

$$\eta^H_{i+1/2,j} = max(\eta_{i+1/2,j}, \eta_{ij+1/2}, \eta_{ij-1/2}, \eta_{i+1j+1/2}, \eta_{i+1j-1/2}), \tag{70}$$

where

$$\eta_{i+1/2,j} = \frac{1}{2}|c_{ij} - c_{i+1j}| + \frac{1}{2}|u_{ij} - u_{i+1j}|. \tag{71}$$

The corresponding added amount of dissipation is then

$$\frac{\eta^H_{i+1/2,j}\Delta q_{i+1/2,j} - \eta^H_{i-1/2,j}\Delta q_{i-1/2,j}}{\Delta x}, \tag{72}$$

where $\Delta q_j = q_R - q_L$ is the difference in biased stencil reconstructions. We find that the above correction works adequately at removing the notch observed in Fig. 3 when applied with a low-order linear Riemann solver. However, the solver described currently is not a true linearization of the Euler equations since the blending of nonlinear center-difference and Riemann reconstruction has no definable corresponding left and right state or linearized Jacobian matrix $\widehat{A}$. To address these issues we make a multidimensional H-correction to the limiter to promote scheme invariance under grid rotation,

$$\Phi^H_{i+1/2,j} = \left(\Phi^2_{i+1/2,j} + max(\Phi^2_{ij+1/2}, \Phi^2_{ij-1/2}, \Phi^2_{i+1j+1/2}, \Phi^2_{i+1j-1/2})\right)^{1/2}. \tag{73}$$

We follow this up by amplifying the limiter at sonic points with large wave speed variation,

$$\Phi^{H\prime}_{i+1/2,j} = \left(\frac{\eta^H_{i+1/2,j}/|\lambda|^H_{max}}{|\lambda|^H_{min}/|\lambda|^H_{max} + \varepsilon}\right)^{1/2} \Phi^H_{i+1/2,j}, \tag{74}$$

which promotes dissipation through the steepest parts of shock waves where the limiter often drops bellow the maximum, resulting is an undesirable region with low dissipation. We then add an amount of dissipation equal to

$$\frac{\Phi^H_{i+1/2,j}\eta^H_{i+1/2,j}\Delta q_{i+1/2,j} - \Phi^H_{i-1/2,j}\eta^H_{i-1/2,j}\Delta q_{i-1/2,j}}{\Delta x}. \tag{75}$$

We find that doing so works reasonably well at mitigating the carbuncle like notch (Fig. 4), but also yields a considerable increase in overall numerical dissipation.

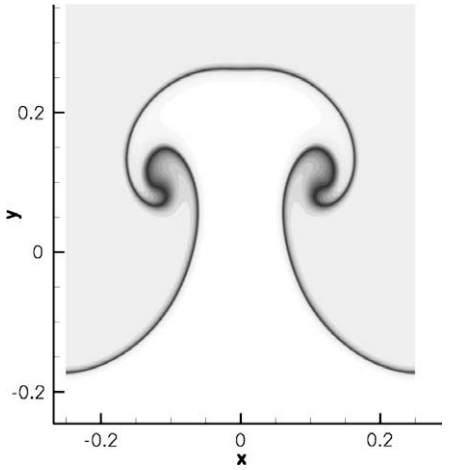

Fig. 4. MORB-Molybdenum Mach 1.5 single cosine mode perturbation Richtmyer–Meshkov instability simulation results with present H-correction for carbuncle implemented for $t = 37$ ms. The carbuncle like notch observed in Fig. 3 is smoothed over.

4.4. One-dimensional test problems

4.4.1. Simple wave

First, to demonstrate how the limiter method behaves on its own we apply it without hybridization to a simple breaking wave in a one meter long periodic slab of mid-ocean ridge basalt (MORB). The initial conditions are continuous and periodic in nature, corresponding to states in tension along the Murnaghan isentrope. For continuous initial conditions, the single phase Euler equations in one dimension yield the solution [13]

$$u(\rho) = \pm \int \frac{c(\rho)}{\rho} d\rho \tag{76}$$

along characteristics defined in space and time from

$$x = t(u \pm c(u)) + f(u). \tag{77}$$

Landau and Lifshitz [13] demonstrate a simple periodic single mode wave solution for isentropes of a perfect gas. The solution is shown to become increasingly steep, eventually forming shocks. For metals described by Mie-Grüneisen equations of state with reference state curves given by a Hugoniot, an analytic equation for isentropes is not generally attainable. However, the use of a Murnaghan isentrope for extending the equation of state for expanded states provides a single isentrope in the form

$$p(\rho, s = s_0) = A\rho^{\alpha} + B. \tag{78}$$

Solution to the Euler equations for this isentrope in terms of velocity is then

$$u(\rho) = \frac{2\sqrt{\alpha A}}{\alpha - 1} \rho^{\frac{\alpha-1}{2}} + const. \tag{79}$$

For our initial conditions we chose a simple sine wave for the initial velocity profile,

$$\begin{aligned} u(x, t = 0) &= U_0 \sin(kx), \\ f(u) &= \tfrac{1}{k} \sin^{-1}(u/U), \end{aligned} \tag{80}$$

with $U_0 = 60.34$ m/s, corresponding to a density variation of $2500.4 \leqslant \rho \leqslant 2659.7$ kg/m^3. Simulation results are seen in Figs. 5 and 6 for $CFL = 0.95$ and $\Delta x = 0.01$ m. For early times the limiter remains relatively small yielding very little numerical dissipation. As the shockwave begins to form at the inflection point the limiter increases locally to introduce the desired character of the upwinding Roe solve, maintaining a relatively smooth solution.

For smooth solutions such as the simple wave before a shock forms, with the use of 4th order SSP RK-4 temporal discretization, the numerical convergence rate of the presently described methodology should be 4th-order. To demonstrate the convergence rate we calculated an approximation to the L_2 error norm in density at $t = 0.5$ ms for various numbers of points while maintaining a fixed CFL of 0.95. To isolate the numerical method we do so without hybridization. The results of the study are given in Table 3. The convergence order is seen to be mesh-size dependent, asymptotically approaching the expected 4th order rate of convergence as the number of points increases.

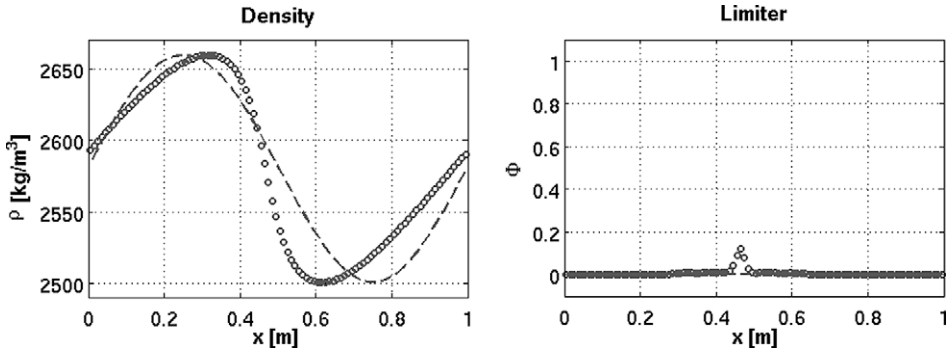

Fig. 5. Simple wave simulation density and limiter profiles at $t = 0.5$ ms. Simulation $CFL = 0.95$ and $\Delta x = 0.01$ m. The dashed line refers to the initial conditions. As the solution progresses in time the wave slowly begins to break, inducing a gradual increase in the limiter locally centered around the steepening inflection point.

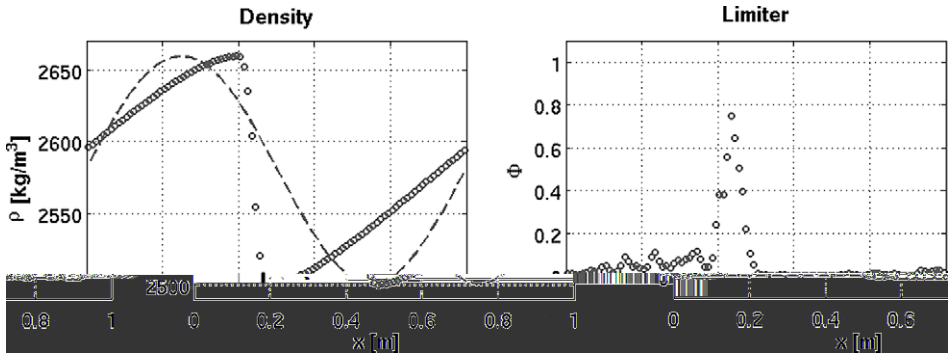

Fig. 6. Simple wave simulation density and limiter profiles at $t = 1$ ms. $CFL = 0.95$ and $\Delta x = 0.01$ m. The dashed line refers to the initial conditions. As time progresses and a shock forms the limiter increases to introduce more dissipation locally, maintaining a relatively smooth flow on either side of the shock.

Table 3
Simple wave solution density L_2 error norm and convergence order for $t = 0.5$ ms. As the grid is refined, the order of convergence is seen to approach the expected 4th order value.

N	L_2 error	L_2 order
50	3.247172e−1	–
80	6.952834e−2	3.2792
100	3.173425e−2	3.5149
120	1.561053e−2	3.8903
150	6.574074e−3	3.8763
200	2.105829e−3	3.9572
300	4.161969e−4	3.9986

4.4.2. Aluminum impact problem

Next we consider a single phase test problem consisting of an impact between two slabs of Aluminum in one dimension [31]. A semi-infinite slab of Aluminum with zero stress, corresponding to ρ_0, p_0, and e_0 given in Table 2, travels leftward at 2000 m/s striking a pre-compressed semi-infinite slab of Aluminum with density $\rho = 4000\ \mathrm{kg/m^3}$ and pressure $p = 7.98$ GPa. Both slabs are modeled as fluids with a single Mie-Grüneisen equation with Hugoniots as reference state curves. The solution to this Riemann problem consist of a reflected and transmitted shock along with a constant pressure and velocity density jump between them.

Fig. 7 presents results at $t = 50\ \mu$s for simulation of the problem with 100 points and an adaptively maintained $CFL = 0.95$. The density, velocity, and pressure all remain relatively smooth. The limiter, plotted bottom right in Fig. 7, demonstrates the necessary increase near the reflected and transmitted shocks. At the density contact the limiter is slightly less active, a desirable result that is a consequence of the nature of the limiter which decreases as numerical diffusion smooths out the flow. Ideally a hybrid switching criterion would indicate when the center-difference scheme is solely adequate to maintain the feature, however, this is hard to achieve this in practice.

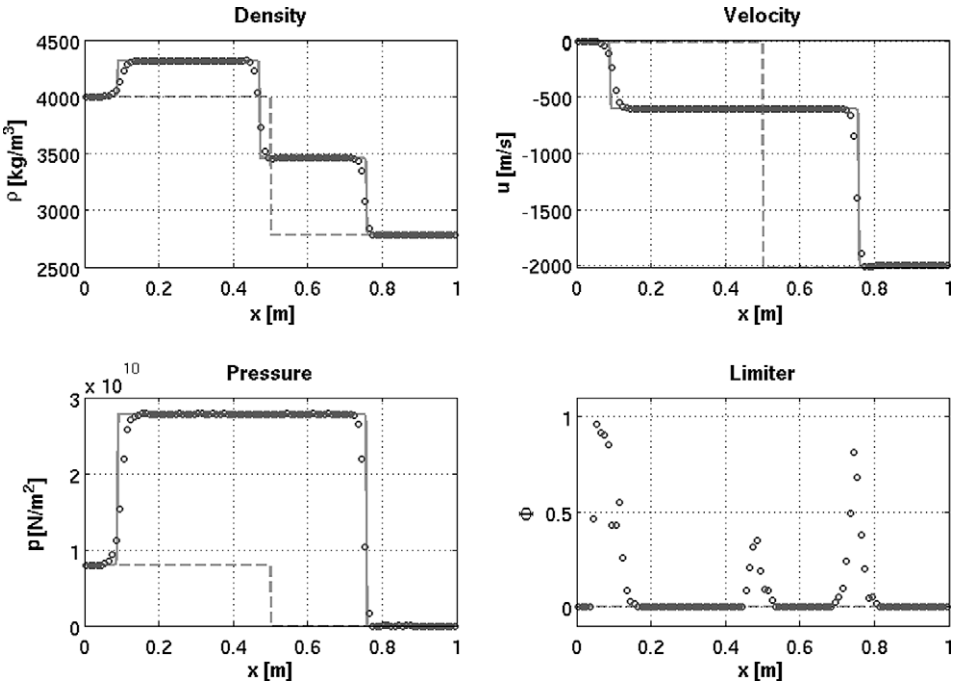

Fig. 7. Results from a one dimensional simulation of an Aluminum impact problem with 100 points and *CFL* = 0.95 at $t = 50$ μs. The dashed line refers to initial conditions and the solid line to the exact solution. The limiter adjusts at the reflected and transmitted shocks and interface, maintaining solution smoothness.

4.4.3. Mach 2.5 MORB-Molybdenum shock-contact problem

In the interest of later making comparison to a two-dimensional Richtmyer–Meshkov instability simulation, we now consider a one dimensional shock-contact multiphase test problem involving two semi-infinite slabs that make diffuse contact at the origin. To the left is Molybdenum and the right MORB, states corresponding to ρ_0, p_0, and e_0. Mach 2.5 shock wave travels through the MORB to the left starting from $x = 0.5$ m. The shock eventually reaches the origin yielding a transmitted shock in the Molybdenum slab and reflected shock back into the MORB. The diffuse contact at the origin is defined by smearing the initial mixture fraction

$$\psi(x, t = 0) = \frac{1}{2} + \frac{1}{2}\tanh(\beta x), \tag{81}$$

where $\beta = 50\ \mathrm{m}^{-1}$ was taken. The states through diffuse contact are given by the ad hoc mixture rule (18).

To keep the contact well within the domain, we perform a simulation in an inertial frame of reference that gives zero velocity between the reflected and transmitted shocks. Results for 100 points and adaptively maintained *CFL* of 0.95 at $t = 0.18$ μs are seen in Fig. 8. Again it is observed that the density, velocity, pressure, and initial mixture fraction maintain smooth profiles.

4.5. Two-dimensional test problems

4.5.1. Planar Richtmyer–Meshkov instability

To demonstrate the methodology in two dimensions, we simulate planar Richtmyer–Meshkov instability involving a single cosine mode perturbation of an interface between Molybdenum and MORB. A Mach 2.5 shock wave travels from top to bottom striking a diffuse interface with initial mixture fraction perturbation described by

$$\psi(x, y, t = 0) = \frac{h_0}{2}\cos(2\pi x/\lambda)[1 + \tanh(\beta(y - y_0))], \tag{82}$$

where the wave length $\lambda = 0.5$ m,$h_0 = 0.05$ m,$y_0 = -0.05$ m, and the factor $\beta = 50\ \mathrm{m}^{-1}$. The ad hoc mixture rule (18) applied to ρ_0, P_0, and E_0 is then used to define the initial states in the diffuse region. The shock begins at position $y = 0.5$ m and travels downward. Unlike the one dimensional or unperturbed problem, the shock deposits vorticity in addition to creating reflected and transmitted shock waves. The vorticity deposited causes the perturbation to grow in time and eventually roll up, making the solution complex in nature.

For the purposes of simulation, a domain of 0.5 m wide by 5 m tall was utilized with periodic boundary conditions in the x-direction. A base grid of 32 by 320 points was used with 3 levels of two times refinement corresponding to an effective

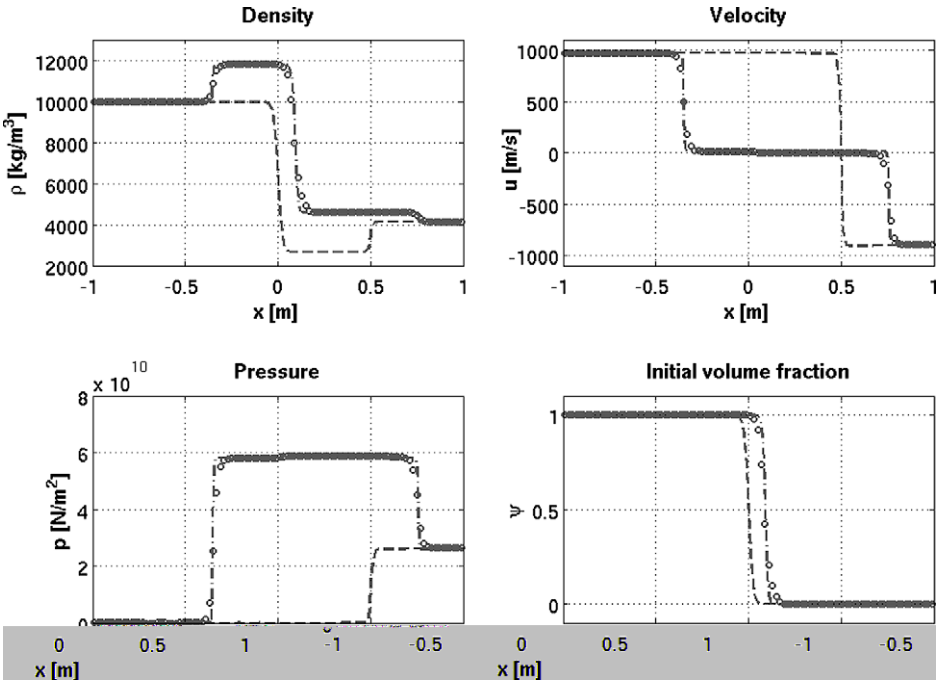

Fig. 8. Mach 2.5 MORB-Molybdenum shock-contact problem centerline density, velocity, pressure, and mixture fraction plots for $t = 0.18$ ms, shortly after shock-interface interaction. Simulation performed with 100 points and $CFL = 0.95$ maintained adaptively. The dashed line refers to initial conditions and the dash-dot line to a simulation with 1000 points. Transmitted and reflected shocks are observed, leaving a stationary contact in between.

resolution of 256 by 2560. For convenience the simulation was performed in a frame of reference that would give zero velocity between the reflected and transmitted shocks if the interface were unperturbed. A *CFL* of 0.9 is maintained adaptively through out the simulation. Fig. 9(a) displays a density contour plot at time $t = 1.9$ ms. Reasonable resolution of features in the roll up is observed. Fig. 9(b) shows where the limiter scheme and purely center-difference schemes are active, denoted by grey and white, respectively. The material interface and coarse-fine adaptive mesh refinement boundaries are tagged for application of the full limiter scheme. Although hard to notice, some asymmetry in the roll up can be observed and is due to asymmetric AMR domain decomposition. To better show how the limiter methodology and solution behave, centerline plots of density, vertical velocity, pressure, and initial mixture fraction are presented in Fig. 10 for $t = 0.18$ ms, not long after shock-interface interaction. The time corresponds to those of the results for the one dimensional shock-contact problem seen in Fig. 8. The features of the centerline for the two-dimensional problem are considerably more complex than those of the associated one dimensional problem.

4.5.2. Planar Richtmyer–Meshkov instability with reshock

Here we take the same initial conditions described in the previous section, but now allow the transmitted shock to reflect off a wall 3.8 m away from the initial interface position of $y = -0.05$ m. The reflected shock eventually reaches the growing perturbed interface, depositing more vorticity and yielding transmitted shocks and reflected expansion waves. Fig. 11 gives Schlieren density contours for time $t = 1.8$ ms as calculated by the current 4th-order method and a purely 3rd-order WENO reconstruction method. The time is well after reshock occurs and demonstrates finer roll up for the present 4th-order methodology.

A plot of the amplitude as a function of time for the initial conditions simulated with 3rd-order WENO reconstruction and present 4th-order methodology is given in Fig. 12. For Richtmyer–Meshkov instability, despite the complexity of the solution, a simple prediction for early time amplitude growth rate can be made. First order linear analysis of an impulsively accelerated incompressible perturbed interface, first carried out by Meshkov [20,26], predicts that the amplitude growth rate is given by

$$\dot{h} = h_0^+ A^+ k \Delta u, \tag{83}$$

where h_0^+ is the post-shock perturbation amplitude, $A^+ = (\rho_2^+ - \rho_1^+)/(\rho_2^+ + \rho_1^+)$ is the post-shock Atwood ratio, $k = 2\pi/\lambda$ is the initial perturbation wave number, and Δu is the change in velocity of the interface imparted by the shock associated with the unperturbed shock-contact problem. Making a comparison to Richtmyer's impulsive theory therefore requires a working definition for perturbation amplitude. Before roll up occurs, one possible way to define the interfaces centerline is

$$y_{cd}(x,t) = \frac{\int_{-\infty}^{\infty} y\psi(x,y,t)(1-\psi(x,y,t))dy}{\int_{-\infty}^{\infty} \psi(x,y,t)(1-\psi(x,y,t))dy}. \tag{84}$$

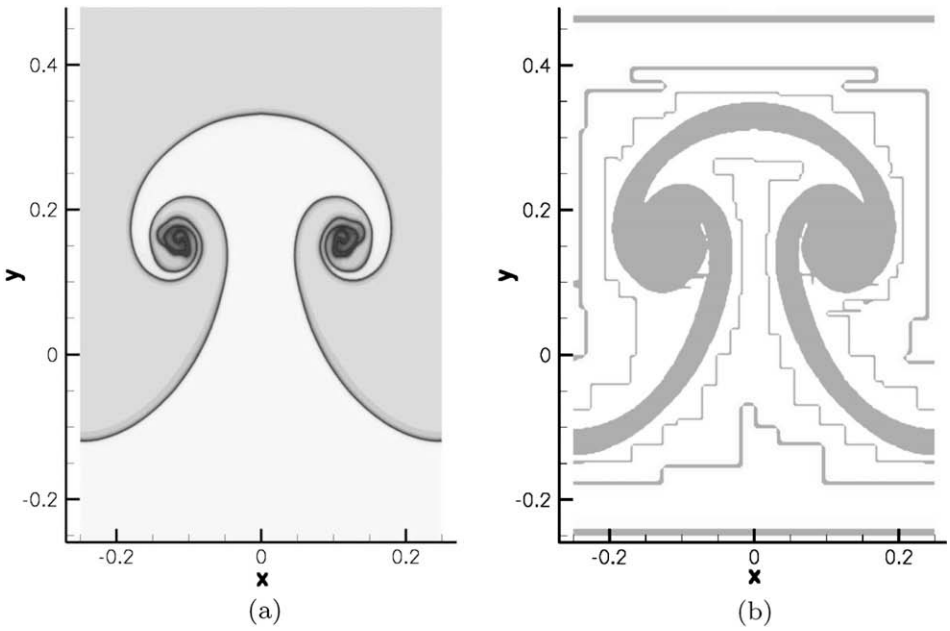

Fig. 9. Mach 2.5 MORB-Molybdenum single mode Richtmyer–Meshkov instability density contour plot (a) and hybrid switching zone plot (b) for $t = 1.9$ ms. Simulation performed with a base grid of 32 by 320 points with 3 levels of two times refinement. Adaptive time stepping was used to maintain a *CFL* of roughly 0.9. The limiter scheme coverage is indicated by grey regions of figure (b), namely at the contact and coarse-fine refinement boundaries.

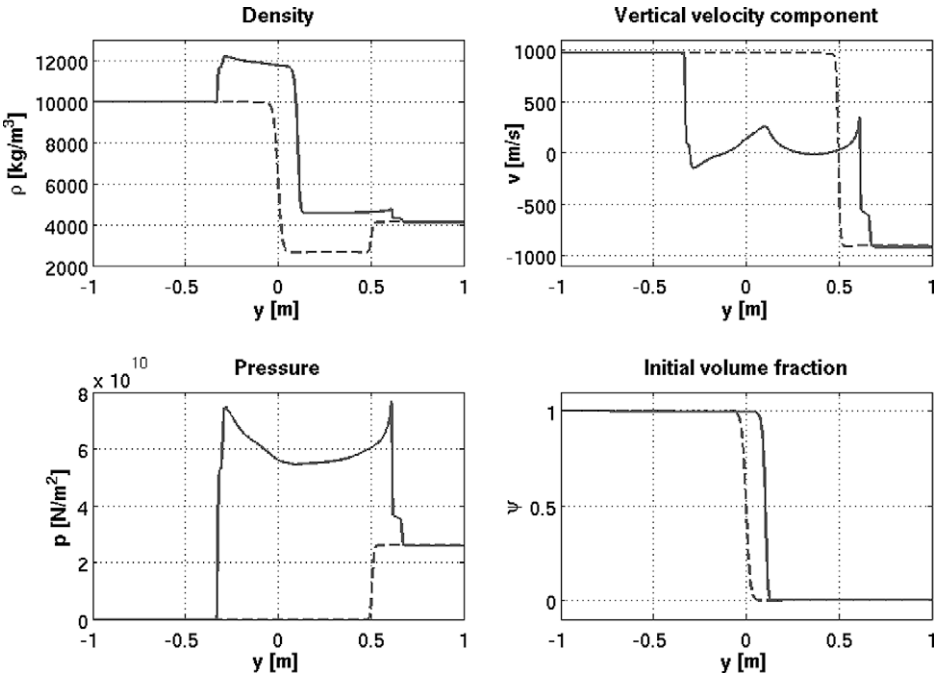

Fig. 10. Mach 2.5 MORB-Molybdenum Richtmyer–Meshkov instability centerline density, velocity, pressure, and scalar mixture fraction plots for $t = 0.18$ ms, shortly after shock-interface interaction. The dashed line refers to initial conditions. The solution structure is considerably more complex than that of the one dimensional shock-contact problem seen in Fig. 8. Transmitted and reflected shocks are observed, but with considerably more variation in properties in between due to multidimensional effects.

The instability amplitude is then simply

$$h(t) = \frac{1}{2}(y_{spike}(t) - y_{bubble}(t)), \tag{85}$$

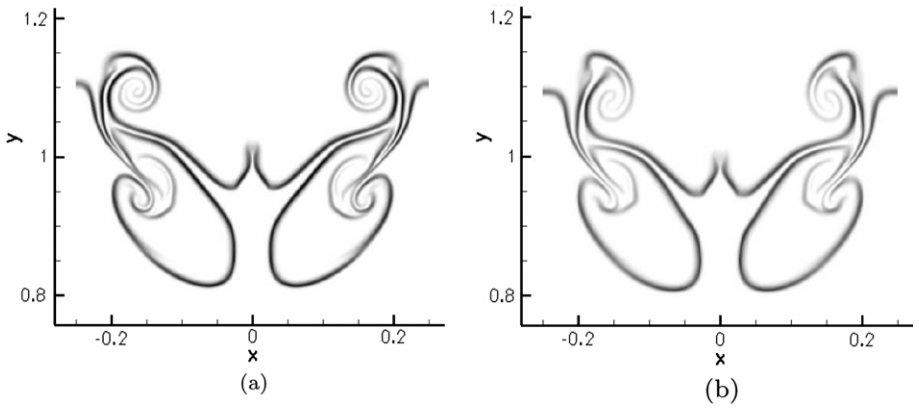

Fig. 11. Mach 2.5 MORB-Molybdenum single mode Richtmyer–Meshkov instability Schlieren contour plot for $t = 1.8$ ms calculated with (a) simulations with present method and (b) primitive third-order WENO reconstruction method. Simulation performed with a base grid of 32 by 320 points with 3 levels of two times refinement. Adaptive time stepping was used to maintain a *CFL* of roughly 0.9. The present scheme demonstrates slightly finer detail in small scale structures.

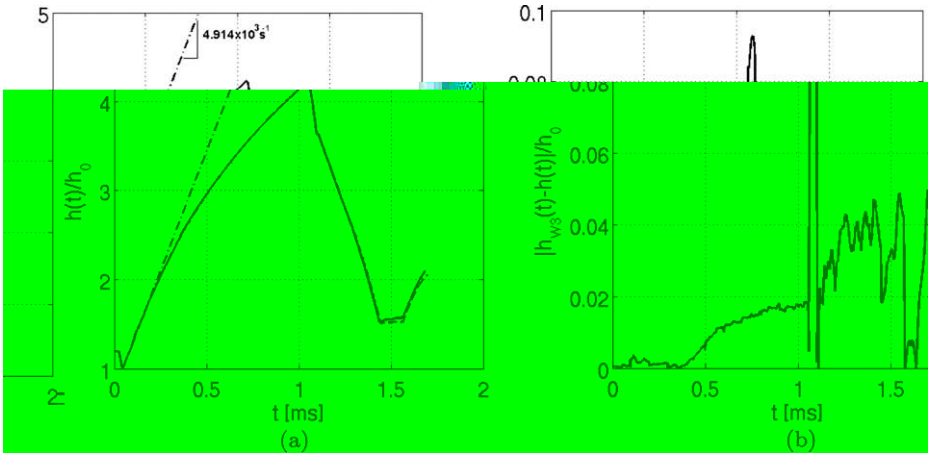

Fig. 12. (a) Mach 2.5 MORB-Molybdenum Richtmyer–Meshkov instability amplitude growth for third-order WENO and present 4th Order methodology, denoted by dashed and solid lines respectively. The dash-dot line represents a fit of data in the linear growth regime. The growth rate obtained is 4.914×10^3 s^{-1}, closely matching the simplified impulsive model of Richtmyer which predicts a growth rate of 5.313×10^3 s^{-1}. (b) The difference in amplitudes as predicted by third-order WENO and present 4th order methodology. After reshock the two methods demonstrate increasing difference in predicted amplitude due to greater dissipation of small scales by the WENO method.

where $y_{spike}(t)$ and $y_{bubble}(t)$ are

$$y_{spike}(t) = max(y_{cd}(x,t)), \quad -\frac{\lambda}{2} < x < \frac{\lambda}{2},$$
$$y_{bubble}(t) = min(y_{cd}(x,t)), \quad -\frac{\lambda}{2} < x < \frac{\lambda}{2}. \tag{86}$$

Making a linear fit of the data for early times yields a calculated impulsive growth rate of 4.914×10^3 s^{-1}. Alternatively, the predicted impulsive growth rate from Eq. (83) is $\dot{h}/h_0^+ = 5.313 \times 10^3$ s^{-1}, which agrees quite well with simulation results despite the simplicity of the model. For times before reshock, the amplitudes calculated with 3rd-order WENO and present 4th-order method agree well. After reshock the measured amplitudes begin to demonstrate discrepancies due to variation in small scales responsible for an important part of vorticity deposition upon reshock [14].

5. Conclusions

With application to the multiphase Euler equations in mind, we have developed a robust limiter methodology inspired by the deviation of WENO weights from ideal that is well suited for hybrid solvers of any spatial order. The limiter generates a smooth transition between the application of a low dissipation scheme in smooth regions and upwinding dissipative scheme

where discontinuities exists, an important property that helps minimize spurious oscillations that can arise in hybrid schemes. Additionally, whereas conservative flux-splitting schemes fail to maintain the fidelity of constant pressure-velocity multiphase flows, the use of such a generalized limiter allows for the tracking of primitive variables which prevent degradation of such solutions.

To demonstrate the practicality of the methodology, we developed a spatially 4th order version for the multiphase Euler equations with special adaption for an isotropic Mie-Grüneisen equation of state in one and two dimensions and implemented it using the California Institute of Technology's VTF (Virtual Test Facility) AMROC [7]. To prevent oscillations in mixtures a set of redundant primitive quantities that depend on density and scalar mixture fraction are tracked. For the low dissipation scheme a 4th-order, skew-symmetric difference scheme is utilized. Upwinding is achieved by a 2nd-order Roe Riemann solver blended in with a limiter given by the deviation of weights associated with a 5th-order WENO. Temporal discretization is achieved by SSP-TVD 3rd order Runge–Kutta.

In one dimension we have successfully applied the scheme to single phase and multiphase flows with shock waves. In each case, the limiter adjusts to introduce dissipation at shocks, maintaining relatively smooth flow on either side. For smooth flows we demonstrated that the 4th order convergence rate is achieved. In two dimensions we applied the solver to simulate Mach 2.5 single mode Richtmyer–Meshkov instability in MORB and Molybdenum modeled by shock-Hugoniot Mie-Grüneisen equations of state. For further validation, comparison of simulation perturbation amplitude growth rate and theoretical impulsive growth rate were made, demonstrating good agreement.

In the future, we plan to apply the methodology to further study Richtmyer–Meshkov instability in solids. Additionally, we simulate problems where solids have elasticity and an underlying Mie-Grüneisen equation of state.

Acknowledgments

This Material is based upon work supported by the Department of Energy National Nuclear Security Administration under Award Number DE-FC52-08NA28613.

References

[1] R. Abgrall, How to prevent pressure oscillations in multicomponent flow calculations: a quasi conservative approach, Journal of Computational Physics 125 (1) (1996) 150–160.
[2] N.A. Adams, K. Shariff, A high-resolution hybrid compact-ENO scheme for shock-turbulence interaction problems, Journal of Computational Physics 127 (1) (1996) 27–51.
[3] G. Allaire, S. Clerc, S. Kokh, A five-equation model for the simulation of interfaces between compressible fluids, Journal of Computational Physics 181 (2) (2002) 577–616.
[4] D.S. Balsara, C.W. Shu, Monotonicity preserving weighted essentially non-oscillatory schemes with increasingly high-order of accuracy, Journal of Computational Physics 160 (2) (2000) 405–452.
[5] M.J. Berger, P. Colella, Local adaptive mesh refinement for shock hydrodynamics, Journal of Computational Physics 82 (1) (1989) 64–84.
[6] M.J. Berger, J.E. Oliger, Adaptive Mesh Refinement for Hyperbolic Partial Differential Equations, 1983.
[7] J. Cummings, M. Aivazis, R. Samtaney, R. Radovitzky, S. Mauch, D. Meiron, A virtual test facility for the simulation of dynamic response in materials, Journal of Supercomputing 23 (1) (2001) 39–50.
[8] M. Dumbser, J.M. Moschetta, J. Gressier, A matrix stability analysis of the carbuncle phenomenon, Journal of Computational Physics 197 (2) (2004) 647–670.
[9] S. Gottlieb, C.W. Shu, E. Tadmor, Strong stability-preserving high-order time discretization methods, SIAM review (2001) 89–112.
[10] D.J. Hill, D.I. Pullin, Hybrid tuned center-difference-WENO method for large eddy simulations in the presence of strong shocks, Journal of Computational Physics 194 (2) (2004) 435–450.
[11] G.S. Jiang, C.W. Shu, Efficient implementation of weighted ENO schemes, Journal of Computational Physics 126 (1996) 202–228.
[12] E. Johnsen, T. Colonius, Implementation of WENO schemes in compressible multicomponent flow problems, Journal of Computational Physics 219 (2) (2006) 715–732.
[13] L.D. Landau, E.M. Lifshitz, Course of theoretical physics, vol. 6, Fluid Mechanics, London, 1987.
[14] M. Latini, O. Schilling, W.S. Don, Effects of WENO flux reconstruction order and spatial resolution on reshocked two-dimensional Richtmyer–Meshkov instability, Journal of Computational Physics 221 (2) (2007) 805–836.
[15] R.J. LeVeque, Numerical Methods for Conservation Laws, Birkhäuser, 1992.
[16] R.J. LeVeque, Finite Volume Methods for Hyperbolic Problems, Cambridge University Press, 2002.
[17] X.D. Liu, S. Osher, T. Chan, Weighted essentially non-oscillatory schemes, Journal of Computational Physics 115 (1) (1994) 200–212.
[18] M. Lombardini, Richtmyer–Meshkov instability in converging geometries, Ph.D. Thesis, 2008.
[19] M.P. Martin, E.M. Taylor, M. Wu, V.G. Weirs, A bandwidth-optimized WENO scheme for the effective direct numerical simulation of compressible turbulence, Journal of Computational Physics 220 (1) (2006) 270–289.
[20] E.E. Meshkov, Instability of the interface of two gases accelerated by a shock wave, Fluid Dynamics 4 (5) (1969) 101–104.
[21] G.H. Miller, E.G. Puckett, A high-order Godunov method for multiple condensed phases, Journal of Computational Physics 128 (1) (1996) 134–164.
[22] P. Moin, K. Mahesh, Direct numerical simulation: a tool in turbulence research, Annual Review of Fluid Mechanics 30 (1) (1998) 539–578.
[23] C. Pantano, R. Deiterding, D.J. Hill, D.I. Pullin, A low-numerical dissipation, patch-based adaptive-mesh-refinement method for large-eddy simulation of compressible flows, Journal of Computational Physics (2006).
[24] S. Pirozzoli, Conservative hybrid compact-WENO schemes for shock-turbulence interaction, Journal of Computational Physics 178 (1) (2002) 81–117.
[25] J.J. Quirk, A contribution to the great Riemann solver debate, International Journal for Numerical Methods in Fluids 18 (6) (1994).
[26] R.D. Richtmyer, Taylor instability in shock acceleration of compressible fluids, Technical Report, LA-1914 (del.), Los Alamos Scientific Lab., N. Mex., 1954.
[27] P.L. Roe, Approximate Riemann solvers, parameter vectors, and difference schemes, Journal of Computational Physics 135 (2) (1997) 250–258.
[28] R. Sanders, E. Morano, M.C. Druguet, Multidimensional dissipation for upwind schemes: stability and applications to gas dynamics, Journal of Computational Physics 145 (2) (1998) 11–537.
[29] C.W. Shu, Institute for Computer Applications in Science, and Engineering. Essentially Non-oscillatory and Weighted Essentially Non-oscillatory Schemes for Hyperbolic Conservation Laws, Lecture Notes in Mathematics-Springer Verlag, 1998.

[30] K.M. Shyue, A fluid-mixture type algorithm for compressible multicomponent flow with van der Waals equation of state, Journal of Computational Physics 156 (1999) 43–88.
[31] K.M. Shyue, A fluid-mixture type algorithm for compressible multicomponent flow with Mie-Gruneisen equation of state, Journal of Computational Physics 171 (2) (2001) 678–707.
[32] E.F. Toro, Riemann Solvers and Numerical Methods for Fluid Dynamics: A Practical Introduction, 2009.